Transmission and transformation of entangled states with high fidelity in a non-Hermitian system

Zan Tang,* Bo Wang,* Tian Chen,*,† and Xiangdong Zhang‡

Key Laboratory of Advanced Optoelectronic Quantum Architecture and Measurements of Ministry of Education, Beijing Key Laboratory of Nanophotonics & Ultrafine Optoelectronic Systems, School of Physics, Beijing Institute of Technology, 100081, Beijing, China

(Received 8 May 2022; accepted 28 October 2022; published 28 November 2022)

The study of non-Hermitian systems has attracted more and more attention, because physical properties in many real systems should be described by non-Hermitian Hamiltonians. Due to the existence of absorption and dissipation, transmission and transformation of entangled states with high fidelity are very difficult to realize in the non-Hermitian systems. How to realize transmission and transformation of entangled states with high fidelity in these dissipative systems becomes an open problem. Here we provide an inverse design scheme for topologically protected channels to solve such a problem. From our scheme, topologically protected channels can be designed according to the requirements for the overlap integrals among the initial states, target states, and eigenstates of the system. As a result, robust transmission and transformation of entangled states with high fidelity can be achieved in the non-Hermitian systems. Our proposed scheme has been demonstrated experimentally using the constructed non-Hermitian quantum walk platform. This work interconnects topology, quantum physics, and non-Hermitian systems, and opens up an avenue for quantum engineering in real systems.

DOI: 10.1103/PhysRevResearch.4.043144

I. INTRODUCTION

The realization of robust transmission and transformation of entangled states with high fidelity is crucial for applications in quantum information, computing, and communications [1,2]. At present, the discussions in this regard mainly focus on Hermitian systems [3–20]. In many real cases, however, physical properties should be described by non-Hermitian Hamiltonians due to inevitable interactions with their surroundings [21–30]. In fact, due to the existence of absorption and dissipation, it is very difficult to achieve transmission and transformation of entangled states with high fidelity in the non-Hermitian systems. The question is whether or how to achieve transmission and transformation of entangled states with high fidelity in these dissipative systems.

In this work, we provide an inverse design scheme to solve the above problem by combining the non-Hermitian quantum physics with topology. In general, quantum states are fragile and easily affected by the environment. Combining these quantum states with topology, they can become robust against external perturbations, which has been demonstrated in the Hermitian systems [11,14,19,20]. However, the discussion of topological entanglement states in the non-Hermitian systems is still lacking, although many interesting topological phenomena associated with edge states have been revealed, e.g., skin effect [31–49], lasing [50–54], and so on. Here, we present a theory to realize transmission and transformation of entangled states with high fidelity in non-Hermitian systems. Our theory is based on the inverse design scheme for topologically protected channels in non-Hermitian systems. The topologically protected channels are designed according to the requirements for the overlap integrals among the initial states, target states, and eigenstates of the system. The scheme has been demonstrated experimentally using our constructed non-Hermitian quantum walk platform.

II. THEORY OF INVERSE DESIGN FOR TOPOLOGICALLY PROTECTED CHANNELS IN NON-HERMITIAN SYSTEMS

Recently, we have provided an inverse design scheme for topologically protected channels to realize nearly perfect transmission and transformation of entangled states in the Hermitian system [19]. However, such a scheme cannot be directly extended to the non-Hermitian system. This is because the inverse design scheme strongly relies on the overlap integral of the system, which has a close relation to the spectral decomposition. The spectral decompositions in the Hermitian case cannot be employed in the non-Hermitian system. In the following, we demonstrate a unique inverse design scheme that can work in the non-Hermitian system.

The evolution process in the non-Hermitian system is shown in Fig. 1(a), in which one component of the entangled state alternately experiences gain and loss and the other travels in vacuum. Such an evolution process can be described by the evolution operator $U_{\text{tot}} = U_T \cdots U_i \cdots U_1$, where U_i is the evolution operator of the ith step. In the first half of each step, the amplitude of the wave function undergoes the amplification when directing to the left-side positions. In contrast, the

*These authors contributed equally to this work.
†chentian@bit.edu.cn
‡zhangxd@bit.edu.cn

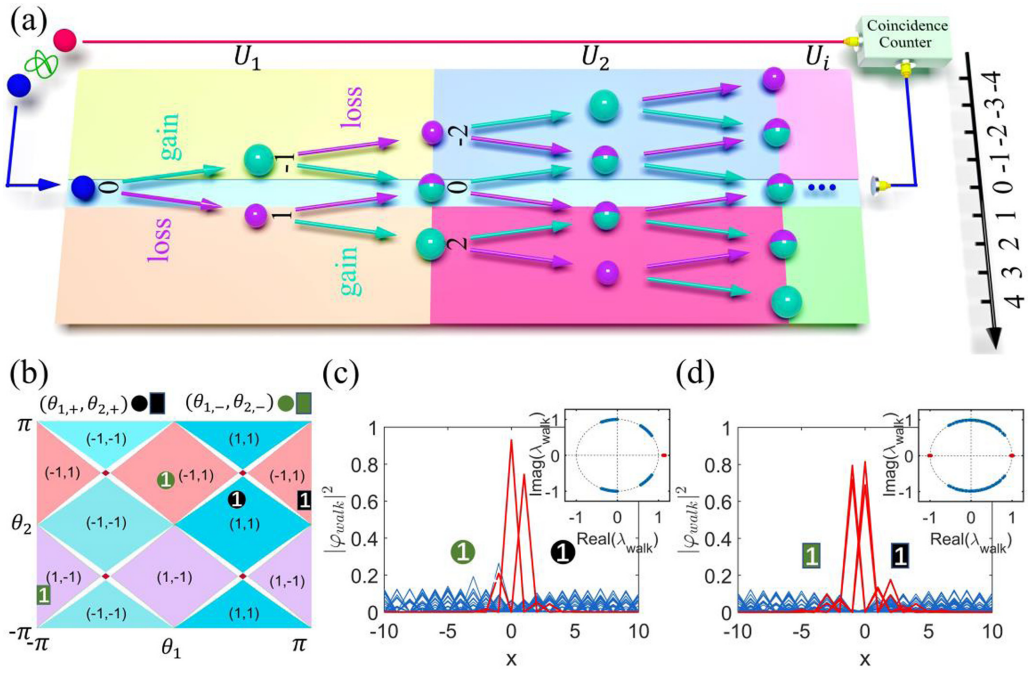

FIG. 1. Construction of a topological channel in a non-Hermitian system. (a) Transmission or transformation of entangled states in the topological channel, which is shown in cyan at the interface. (b) The topological phases are identified by (v_0, v_π) in $U_{\text{walk},i}$. The green and black circles (rectangles) denote the rotation angles in the regions with $0 \leqslant x \leqslant N_x$ ($-N_x \leqslant x < 0$) for the transmission (transformation) of entangled states at the first step. The distribution of eigenstates in $U_{\text{walk},1}$ ($U_{\text{walk}}|\varphi_{\text{walk}}\rangle = \lambda_{\text{walk}}|\varphi_{\text{walk}}\rangle$) for the transmission (c) or transformation (d). Insets in (c,d) show the eigenspectra of $U_{\text{walk},1}$. Red: topological boundary states; blue: bulk states.

amplitude of the wave function is reduced when directing to the right-side positions. In the second half of each step, the amplification and reduction are exchanged. The amplitude of the wave function traveling to the left side is reduced and that to the right side is amplified. With this alternating amplification and reduction, a non-Hermitian system with parity-time symmetry can be constructed [32,33,45,55,56]. At each step, we can create two regions belonging to different topological phases, and build a channel at their interface. The quantum states can be transmitted along the channel.

The transmission and transformation of quantum states along the channel can be regarded as a scattering process, which can be further regarded as a discrete-time quantum walk (QW) process. A representative non-Hermitian QW with parity-time symmetry is $U_{\text{walk},i} = GSR[\theta_{2,\pm}(i)]G^{-1}SR[\theta_{1,\pm}(i)]$ [25,47,48]. Here $G = \sum_x |x\rangle\langle x| \otimes \begin{pmatrix} e^r & 0 \\ 0 & e^{-r} \end{pmatrix}$ is the gain-loss operator, where the superscript r is the gain-loss strength. Under the action of G, the wave function with the coin state $|0\rangle = (1,0)^T$ [$|1\rangle = (0,1)^T$] is amplified (reduced). The state $|x\rangle$ denotes the position in the QW. A conditional shift operator S is $S = \sum_x |x+1\rangle\langle x| \otimes |0\rangle\langle 0| + |x-1\rangle\langle x| \otimes |1\rangle\langle 1|$, and $R[\theta_{m,\pm}(i)] = e^{-i\theta_{m,\pm}(i)\sigma_y/2}\sigma_z$ ($m = 1, 2$) represents the coin operator acting on the coin state. For this QW, topological phases are characterized by topological invariants (v_0, v_π), which come from the summation and subtraction of the Zak phases for $U_{\text{walk},i}$ and the time-shifted version of $U_{\text{walk},i}$ [25,48]. Topological phases are shown in Fig. 1(b). When rotation angles $(\theta_{1,-}, \theta_{2,-})$ for positions $-N_x \leqslant x < 0$ and $(\theta_{1,+}, \theta_{2,+})$ for $0 \leqslant x \leqslant N_x$ are chosen from different topological phases, the topologically protected channel is constructed at $x = 0$.

Generally, even though the localized probability in the topological channel is obvious, the initial states are changed considerably after passing through the topological channel without any design [11,14]. If we can construct the non-Hermitian QW whose eigenmodes in the channel support the transmission of the initial state, the scattering loss can be overcome and the transmission with high fidelity can be realized. The design of the non-Hermitian QW with specific eigenmodes requires us to do spectral decomposition, which is greatly different from the Hermitian systems. The right and left biorthogonal eigenstates $|\varphi_i\rangle$ and $|\chi_i\rangle$ ($U|\varphi_i\rangle = \lambda_i|\varphi_i\rangle$ and $U^\dagger|\chi_i\rangle = \lambda_i^*|\chi_i\rangle$) are chosen, and satisfied by the biorthogonal relation $\langle\chi_i|\varphi_j\rangle = 0 (i \neq j)$. The completeness relation in the non-Hermitian case is $\frac{\sum_{i=1}^n |\varphi_d i\rangle\langle\chi_i|}{\langle\chi_i|\varphi_i\rangle=I}$. With the normalized right (left) eigenstate $\frac{|\varphi_i\rangle}{\sqrt{\langle\chi_i|\varphi_i\rangle}}$ ($\frac{|\chi_i\rangle}{\sqrt{\langle\chi_i|\varphi_i\rangle}}$), the initial state $|\phi_m\rangle$ after one step of evolution changes to

$$
\begin{aligned}
U|\phi_m\rangle &= \sum_{i=1}^{n} \lambda_i \frac{|\varphi_i\rangle\langle\chi_i|}{\langle\chi_i\,|\,\varphi_i\rangle}|\phi_m\rangle \\
&= \lambda_1 \frac{|\varphi_1\rangle\langle\chi_1|}{\langle\chi_1\,|\,\varphi_1\rangle}|\phi_m\rangle + \lambda_2 \frac{|\varphi_2\rangle\langle\chi_2|}{\langle\chi_2\,|\,\varphi_2\rangle}|\varphi_m\rangle \\
&\quad + \cdots \lambda_n \frac{|\varphi_n\rangle\langle\chi_n|}{\langle\chi_n\,|\,\varphi_n\rangle}|\varphi_m\rangle. \qquad (1)
\end{aligned}
$$

The overlap integral of the eigenstate and the target quantum state $|\phi_l\rangle$ is defined as $P_{l,m}^i = |\langle\phi_l|\lambda_i \frac{|\varphi_i\rangle\langle\chi_i|}{\langle\chi_i|\varphi_i\rangle}|\phi_m\rangle|$ to evaluate the transportation. The large value of the overlap

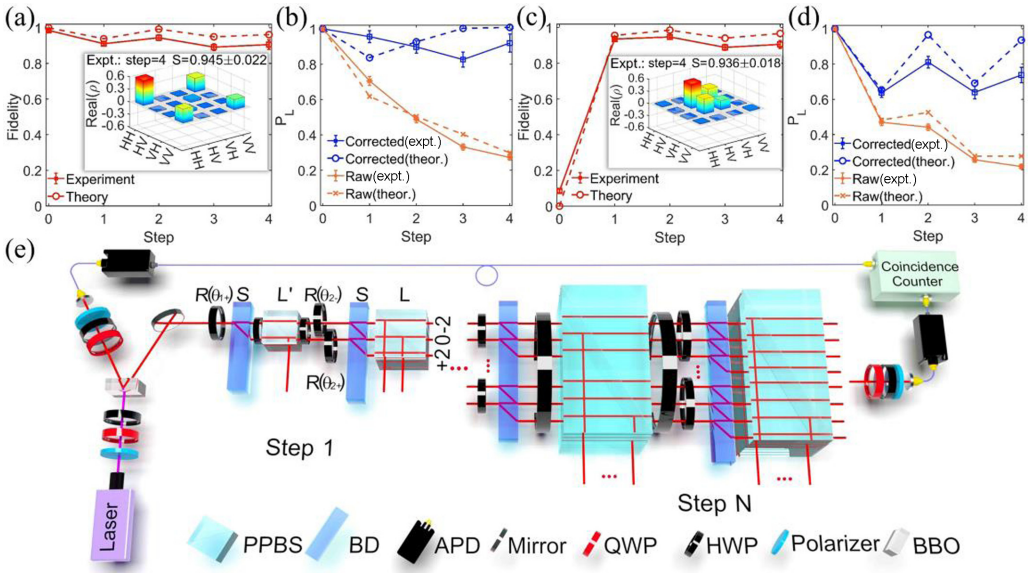

FIG. 2. Perfect transmission and transformation in non-Hermitian QWs. (a,b) The fidelity and localization at the channel in the transmission of $|\phi_1\rangle$. (c,d) The fidelity and localization at the channel in the transformation from $|\phi_1\rangle$ to $|\phi_3\rangle$. Dashed line, theoretical results; solid line, experimental results. All error bars refer to ± 1 s.d. estimated from Poissonian photon-counting statistics. Insets in (a,c) show the experimentally obtained density matrix at the fourth step. The similarity S indicates the degree of agreement between the experiment and theory. (e) Many steps of non-Hermitian QWs in the experiment. The evolution at the ith step is $U_{\text{exp},i} = LSR[\theta_{2,\pm}(i)]L'SR[\theta_{1,\pm}(i)]$.

integral can be obtained in two ways. The first way is from the large overlap among the initial state, the eigenstates of the system, and the final state. It corresponds to a successful transportation of the initial state for the eigenstate of the system supports the transmission very well, which is also our goal in the design. The second way comes from the zero or nearly zero $\langle\chi_i|\varphi_i\rangle$ in the denominator. This situation often emerges in the non-Hermitian system possessing exception points, which leads to the self-orthogonal phenomenon with $\langle\chi_i|\varphi_i\rangle = 0$. Such an abnormally large overlap integral can't be used in the transmission or transformation of states.

When the maximum entangled states $|\phi_1\rangle = \frac{1}{\sqrt{2}}(|00\rangle + |11\rangle)$, $|\phi_2\rangle \frac{1}{\sqrt{2}} = (|00\rangle - |11\rangle)$, $|\phi_3\rangle = \frac{1}{\sqrt{2}}(|01\rangle + |10\rangle)$, and $|\phi_4\rangle = \frac{1}{\sqrt{2}}(|01\rangle - |10\rangle)$ are chosen as the initial states, the first component of the entangled states is sent into the topological channel in $U_{\text{walk},i}$, and the other component of the entangled states is sent into vacuum I. The evolution operator for the ith step is $U_i = U_{\text{walk},i} \otimes I$. To design a non-Hermitian QW supporting the transmission or transformation, the overlap integral involving the target state and the input state is calculated by sweeping points in $[-\pi,\pi]$ at the interval of $\pi/32$ for rotation angles $\theta_{1,\pm}$ and $\theta_{2,\pm}$. Then, the rotation angles $(\theta_{1,+}, \theta_{2,+})$ and $(\theta_{1,-}, \theta_{2,-})$ with a large overlap integral are picked at this step, and these rotation angles are indeed from different topological phases. Here the value N_x is taken as $N_x = 20$, which is large enough for the evolution within eight steps. This inverse design process is repeated in each step and the rotation angles $\theta_{1(2),\pm}$ are thus obtained.

The rotation angles for the first step of transmission of $|\phi_1\rangle$ and transformation from $|\phi_1\rangle$ to $|\phi_3\rangle$ are shown in Fig. 1(b). The corresponding distributions of eigenstates have been presented in Figs. 1(c) and 1(d), respectively. Topological edge states are shown in red at the interface ($x = 0$), and the corresponding isolated eigenvalues are also observed in the insets. These results show that the channel at $x = 0$ is topologically protected. Moreover, the rotation angles can be optimally chosen by the inverse design process, and to achieve transmission or transformation of entangled states in the channel with both high fidelity and high efficiency. Figures 2(a) and 2(c) show the theoretical results (dashed lines) for realization of high-fidelity transmission of $|\phi_1\rangle$ and transformation from $|\phi_1\rangle$ to $|\phi_3\rangle$, respectively. The details of the rotation angles have been provided in Appendix A. During the transmission or transformation, the fidelity averaging with four steps is higher than 90%. The oscillatory behaviors of fidelities in Figs. 2(a) and 2(c) are due to the changes of eigenmodes with the rotation angle at each step, which result in some deviations between the actual optimized results and the ideal cases.

In addition to the high fidelity, the scattering loss can also be controlled to be relatively small and leads to strong localization at the topological channel. Due to the gain effect in the non-Hermitian QW, the summation of probability at each step might be larger than 1 and is called "corrected probability" [33]. The blue dashed lines in Figs. 2(b) and 2(d) represent the corrected probabilities in the topological channel during the transmission and transformation, respectively. The mean values of corrected probability averaging with four steps in the channel are both larger than 0.7. Here, only one gain-loss strength ($r = 0.076$) is considered. The nearly perfect transmission of entangled states with other gain-loss strengths has been presented in Appendix A. The perfect transformation from $|\phi_1\rangle$ to other entangled states is available in Appendix B. Detailed analysis about the localization has been shown in Appendix C.

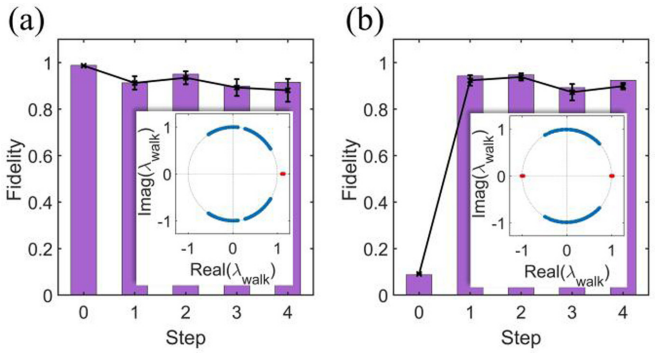

FIG. 3. The robustness in the transmission and transformation of entangled states. (a) The fidelity of transmission of $|\phi_1\rangle$ against disorder. (b) The fidelity for transformation from $|\phi_1\rangle$ to $|\phi_3\rangle$. The purple bars represent the cases without disorder, and the black cross dots represent those with disorder. Inset, eigenvalues $\lambda_{\text{walk},1}$ with disorder. Error bars indicate the standard deviation.

III. EXPERIMENTAL DEMONSTRATION OF PERFECT TRANSMISSION AND TRANSFORMATION OF ENTANGLED STATES

The experimental setup for the non-Hermitian QW with a topologically protected channel is shown in Fig. 2(e). Polarization bell states $|HH\rangle + e^{i\alpha}|VV\rangle$ are generated from a spontaneous parametric down-conversion source. Now, we study transportation of these entangled states in the topologically protected channel. The coin states $|0\rangle$ and $|1\rangle$ in the non-Hermitian QW are encoded in the horizontal $|H\rangle$ and vertical $|V\rangle$ polarization states of the beam. The gain and loss are experimentally realized in an equivalent way, where a smaller (larger) loss in the beam with one (another) polarization is regarded as a gain (loss). The one step evolution operator is $U_{\text{exp},i} = l_1 l_2 U_{\text{walk},i} = LSR[\theta_{2,\pm}(i)]L'SR[\theta_{1,\pm}(i)]$ in which the equivalent gain-loss operators are $L = \begin{pmatrix} l_1 & 0 \\ 0 & l_2 \end{pmatrix}$ and $L' = \begin{pmatrix} l_2 & 0 \\ 0 & l_1 \end{pmatrix} (0 \leqslant l_1, l_2 \leqslant 1,\ l_1 \neq l_2)$. The gain-loss strength is $r = \frac{1}{2}\ln(l_1/l_2)$. The operator L is implemented by using a partially polarizing beam splitter (PPBS), and L' is realized by the HWP (half-wave plate)-PPBS-HWP combination.

The conditional shift operator S is realized by a birefringent crystal beam displacer (BD). Output positions on the lateral section of the BD correspond to positions in the QW. The rotation operator $R[\theta_{1(2),\pm}(i)]$ is implemented by the HWP. The topological channel can be constructed by applying different HWPs for positions $-N_x \leqslant x < 0$ and $0 \leqslant x \leqslant N_x$.

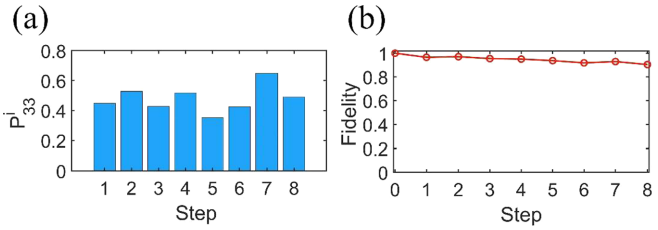

FIG. 5. Theoretical results of the transmission of the entangled state $|\phi_3\rangle$. (a) The overlap integrals. (b) The fidelity.

In the experiment, one photon travels in vacuum, and the other passes through the topological channel. The coincidence measurement is performed at the end. More experimental details are described in Appendix D.

The experimental results of fidelity for the transmission of $|\phi_1\rangle$ are shown in Fig. 2(a); they are basically the same as the theoretical results, and the mean value of fidelity averaging with four steps is about 91.6%. For quantitative comparison, the similarity S is defined as $S[\rho_{\text{th}}, \rho_{\text{ex}}] = tr\sqrt{\rho_{\text{th}}^{1/2}\rho_{\text{ex}}\rho_{\text{th}}^{1/2}}$, where ρ_{th} (ρ_{ex}) represents the theoretical (experimental) density matrix. The value $S = 0.945 \pm 0.022$ is obtained at the fourth step. The localization at the topological channel is provided in Fig. 2(b). Here, the "raw probability" is defined by dividing the coincidence count by the total number of photon pairs before entering the system [33]. The experimental raw probabilities at the topological channel are shown as the orange solid line, and the corresponding theoretical values obtained from $U_{\text{exp},i}$ are presented as the orange dashed line for comparison. The raw probability (orange) is linked to the corrected probability (blue) by multiplying a correction factor $(l_1 l_2)^{2t}$ for the corresponding step t. Large corrected probabilities (blue solid line) at the channel are shown to verify the high efficiency in the transmission. It should be pointed out that the experimental results with four steps are sufficient to display the phenomenon, and we does not need more steps in the experiment. Moreover, the nearly perfect transformation from $|\phi_1\rangle$ to $|\phi_3\rangle$ has also been realized experimentally. The average fidelity of $|\phi_3\rangle$ reaches 91.7% after the transformation, and the similarity at the fourth step is $S = 0.936 \pm 0.018$; see Fig. 2(c). In Fig. 2(d), the localization at the topological channel is presented. Large corrected probabilities (blue solid) at the channel are provided to show the high efficiency in the transformation. More experimental results are available in Appendix D.

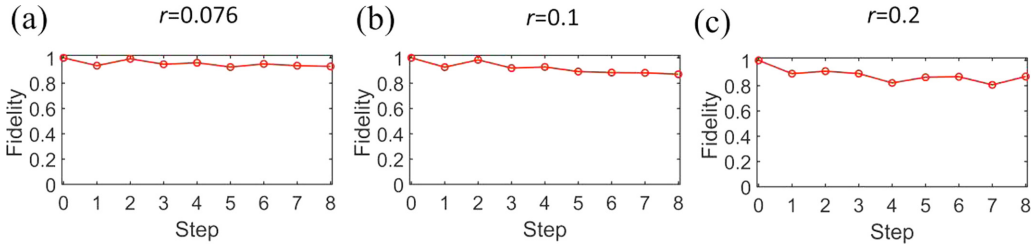

FIG. 4. The fidelity in the transmission of $|\phi_1\rangle$ with different gain-loss strengths. (a) The gain-loss strength is $r = 0.076$. (b) The gain-loss strength is $r = 0.1$. (c) The gain-loss strength is $r = 0.2$.

TABLE I. $\theta_{1,\pm}$ and $\theta_{2,\pm}$ of $U_{\text{walk},i}$ for $r = 0.076$ (1), $r = 0.1$ (2) and $r = 0.2$ (3).

1	$i=1$	$i=2$	$i=3$	$i=4$	$i=5$	$i=6$	$i=7$	$i=8$
$(\theta_{1,+},\theta_{2,+})$	$(\frac{7\pi}{16},\frac{4\pi}{16})$	$(\frac{-7\pi}{16},\frac{-3\pi}{16})$	$(\frac{9\pi}{16},\frac{-11\pi}{16})$	$(\frac{7\pi}{16},\frac{-5\pi}{16})$	$(\frac{-7\pi}{16},\frac{-5\pi}{16})$	$(\frac{-9\pi}{16},\frac{-12\pi}{16})$	$(\frac{9\pi}{16},\frac{-6\pi}{16})$	$(\frac{7\pi}{16},\frac{-10\pi}{16})$
$(\theta_{1,-},\theta_{2,-})$	$(\frac{-1\pi}{16},\frac{7\pi}{16})$	$(\frac{14\pi}{16},\frac{-5\pi}{16})$	$(\frac{-15\pi}{16},\frac{-6\pi}{16})$	$(\frac{-9\pi}{16},\frac{-10\pi}{16})$	$(\frac{-13\pi}{16},\frac{-9\pi}{16})$	$(\frac{-1\pi}{16},\frac{-10\pi}{16})$	$(\frac{2\pi}{16},\frac{-9\pi}{16})$	$(\frac{-12\pi}{16},\frac{-7\pi}{16})$
2	$i=1$	$i=2$	$i=3$	$i=4$	$i=5$	$i=6$	$i=7$	$i=8$
$(\theta_{1,+},\theta_{2,+})$	$(\frac{7\pi}{16},\frac{4\pi}{16})$	$(\frac{-7\pi}{16},\frac{-3\pi}{16})$	$(\frac{9\pi}{16},\frac{-11\pi}{16})$	$(\frac{7\pi}{16},\frac{-5\pi}{16})$	$(\frac{-7\pi}{16},\frac{-5\pi}{16})$	$(\frac{-9\pi}{16},\frac{-12\pi}{16})$	$(\frac{9\pi}{16},\frac{-6\pi}{16})$	$(\frac{7\pi}{16},\frac{-10\pi}{16})$
$(\theta_{1,-},\theta_{2,-})$	$(\frac{-1\pi}{16},\frac{7\pi}{16})$	$(\frac{14\pi}{16},\frac{-5\pi}{16})$	$(\frac{-15\pi}{16},\frac{-6\pi}{16})$	$(\frac{-9\pi}{16},\frac{-10\pi}{16})$	$(\frac{-13\pi}{16},\frac{-9\pi}{16})$	$(\frac{-1\pi}{16},\frac{-10\pi}{16})$	$(\frac{2\pi}{16},\frac{-19\pi}{32})$	$(\frac{-12\pi}{16},\frac{-6\pi}{16})$
3	$i=1$	$i=2$	$i=3$	$i=4$	$i=5$	$i=6$	$i=7$	$i=8$
$(\theta_{1,+},\theta_{2,+})$	$(\frac{7\pi}{16},\frac{5\pi}{16})$	$(\frac{-7\pi}{16},\frac{-1\pi}{16})$	$(\frac{9\pi}{16},\frac{-11\pi}{16})$	$(\frac{15\pi}{32},\frac{-11\pi}{32})$	$(\frac{-7\pi}{16},\frac{-12\pi}{16})$	$(\frac{-8\pi}{16},\frac{-10\pi}{16})$	$(\frac{9\pi}{16},\frac{31\pi}{32})$	$(\frac{7\pi}{16},\frac{-1\pi}{32})$
$(\theta_{1,-},\theta_{2,-})$	$(\frac{-15\pi}{16},\frac{7\pi}{16})$	$(\frac{15\pi}{16},\frac{-4\pi}{16})$	$(\frac{-8\pi}{16},\frac{-10\pi}{16})$	$(\frac{-7\pi}{16},\frac{-5\pi}{16})$	$(\frac{-3\pi}{16},\frac{-5\pi}{16})$	$(\frac{1\pi}{32},\frac{-10\pi}{16})$	$(\frac{4\pi}{16},\frac{-10\pi}{16})$	$(\frac{1\pi}{16},\frac{-13\pi}{32})$

IV. ROBUSTNESS

To test the robustness in the transmission of entangled states, the static disorder in the system is introduced by adding a random angle $\delta\theta$ to θ_1 and θ_2 ($\theta_{1,\pm}+\delta\theta, \theta_{2,\pm}+\delta\theta$), where the degree of disorder $\delta\theta$ is chosen randomly from the interval $(-0.063\pi, 0.063\pi)$ in a uniform distribution. Ten groups of different rotation angles are randomly selected in experiment. The solid line in Fig. 3(a) displays the experimental results for the fidelity of $|\phi_1\rangle$. Comparing it with that without disorder (column bars), we find little difference among them. The bound states (red dots) still exist when the disorder is introduced [see the inset of Fig. 3(a)]. In a similar way, we also demonstrate the robustness of transformation from $|\phi_1\rangle$ to $|\phi_3\rangle$ [Fig. 3(b)]. In Appendix E, similar topological phenomena can be observed when $\delta\theta$ increases. The transmission and transformation of entangled states without topological channel are also provided for comparison, where very low fidelities show the importance of the topological channel in our design.

V. DISCUSSION AND CONCLUSIONS

The discussions above only focus on the case that one part of the entangled states is sent into the topological channel in the non-Hermitian QW, and the other part of the entangled states travels in vacuum. In fact, the inverse design scheme is also suitable for the case that all entangled photons walk along the topological channels. In Appendix F, we have shown that two parts of the entangled states are sent into the inverse-designed topological channels. The nearly perfect transmission of the entangled state can also be realized.

Here, we emphasize again that the inverse design method used in this work is not an extension of the Hermitian case. In fact, the core of our inverse design method is to obtain the large overlap integrals among the initial states, target states, and eigenstates of the system. The spectral decomposition is provided in aid of analysis, which is totally different between the Hermitian and non-Hermitian systems. To accommodate the discussion in non-Hermitian cases, the right and left biorthogonal eigenstates are chosen. These biorthogonal eigenstates satisfy the biorthogonal relation and lead to a specific completeness relation. None of the above appear in the Hermitian cases.

In conclusion, we have presented theoretically an inverse design scheme for the non-Hermitian topological channel. The topological channels have been designed according to the large overlap integrals among the initial states, target states, and eigenstates of the system. Then, the robust transmission and transformation of entangled states with high fidelity have been realized in these channels. The corresponding experiments using the constructed non-Hermitian quantum walk platform have been performed to demonstrate the theoretical schemes. Although the present work has been implemented in free space, the idea of the combination of the inverse design and the non-Hermitian topology can be extended to other systems, e.g., waveguides, integrated chips, and so on. Moreover, the present work only considers one specific non-Hermitian system possessing parity-time symmetry; however, the design method can be employed to a generalized non-Hermitian system. The successful inverse design depends on the overlap integral and related spectral decomposition, which is applicable to general non-Hermitian systems. Our studies pave a way to achieve the scalable quantum information process and quantum engineering in reality [57–74].

ACKNOWLEDGMENTS

This work was supported by the National key R & D Program of China under Grant No. 2017YFA0303800 and the National Natural Science Foundation of China (Grants No. 91850205 and No. 11974046).

APPENDIX A: STUDY OF TRANSMITTING $|\phi_1\rangle$ WITH DIFFERENT GAIN-LOSS STRENGTHS AND TRANSMISSION BEHAVIORS OF DIFFERENT ENTANGLED STATES

In the main text, the transmission of the entangled state $|\phi_1\rangle$ is provided with the gain-loss strength $r = 0.076$. Herein, the theoretical results of the transmission of $|\phi_1\rangle$ with different

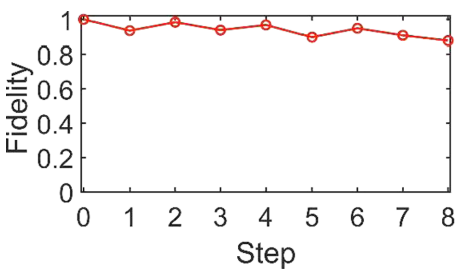

FIG. 6. The fidelity in the transmission of the entangled state $\frac{1}{2}|00\rangle + \frac{\sqrt{3}}{2}|11\rangle$.

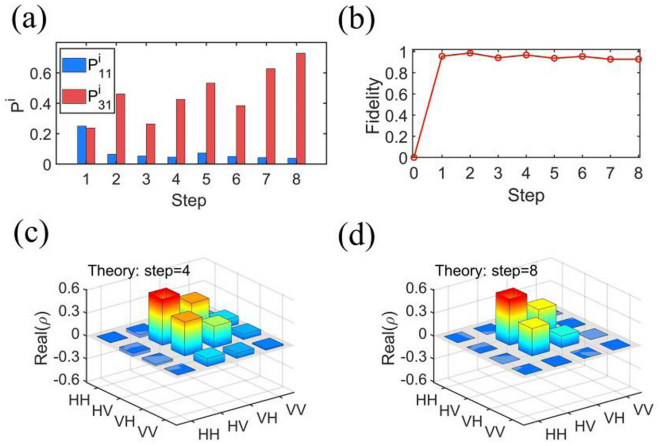

FIG. 7. Theoretical results of the transformation of entangled states in the non-Hermitian QW. (a) The overlap integral $P^i_{3,1}$ of the transformation of entangled states from $|\phi_1\rangle$ to $|\phi_3\rangle$ within eight steps. (b) The fidelity between the output state and $|\phi_3\rangle$. (c,d) Theoretical results of the density matrix at the fourth and eighth steps. The gain-loss strength is taken as $r = 0.076$.

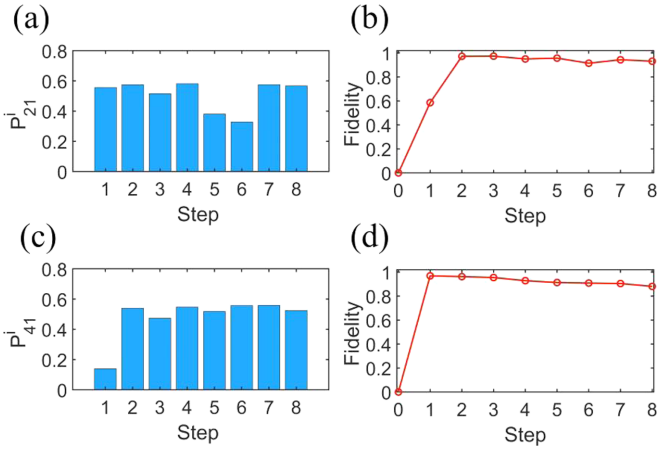

FIG. 8. Theoretical results of the transformation of entangled states. (a,b) Transformation of entangled states from $|\phi_1\rangle$ to $|\phi_2\rangle$. (c,d) Transformation of entangled states from $|\phi_1\rangle$ to $|\phi_4\rangle$. (a,c), overlap integrals. (b,d), the fidelity between the output state and the target states.

gain-loss strengths are also addressed; see Fig. 4. Even though the gain-loss strength r increases, the perfect transmission of the entangled state $|\phi_1\rangle$ can also be achieved. The fidelity still maintains a high value. To reach such a perfect transmission, the inverse design method is also employed. The specific rotation angles of each step are listed in Table I. When $r = 0.076$, the fidelity averaging over eight steps is 94.8%. When $r = 0.1$, the fidelity averaging over eight steps is 91.1%. When the gain-loss strength r increases to 0.2, the average value of fidelity over eight steps is approximately 86.8%.

Not only $|\phi_1\rangle$, but other entangled states can also be transmitted perfectly through the inverse design. We have also carried out theoretical calculations on the transmission of the entangled state $|\phi_3\rangle$. The inverse design method is also employed. The optimal rotation angles of each step are listed in Table II. Figures 5(a) and 5(b) show the theoretical results of the transmission of the entangled state $|\phi_3\rangle$. It can be clearly seen that the overlap integral $P^i_{3,3}$ has always maintained a high value, and the average fidelity of eight steps is equal to 94.1%.

In addition to the maximum entangled state, our method is also applicable to the nonmaximum entangled state. The entangled state $\frac{1}{2}|00\rangle + \frac{\sqrt{3}}{2}|11\rangle$ is chosen. The inverse design method is also employed. The optimal rotation angles of each step are listed in Table III. The transmission of this state is shown in Fig. 6. The red dots in Fig. 6 represent the fidelity whose average value over eight steps is approximately 93.1%. The results above show that the perfect transmission of the nonmaximum entangled state is still achieved.

APPENDIX B: PERFECT TRANSFORMATION OF ENTANGLED STATES FROM $|\phi_1\rangle$ TO $|\phi_2\rangle$, $|\phi_3\rangle$, AND $|\phi_4\rangle$

By using the inverse design method, we can not only realize the perfect transmission of entangled states, but also achieve the nearly perfect transformation of entangled states. For the transformation of entangled states, the initial state and the target state are not the same; $|\phi_l\rangle \neq |\phi_m\rangle$. We select the initial state $|\phi_m\rangle = |\phi_1\rangle = \frac{1}{\sqrt{2}}(|00\rangle + |11\rangle)$ and the target state $|\phi_l\rangle = |\phi_3\rangle = \frac{1}{\sqrt{2}}(|01\rangle + |10\rangle)$. To realize the perfect transformation, we optimize the overlap integral $P^i_{l,m}$ through scanning rotation angles $\theta_{1,\pm}$ and $\theta_{2,\pm}$ within the range $[-\pi, \pi]$ at the interval $\pi/32$. Then the output state at this step is treated as the initial state of the next step to repeat the optimization again. The corresponding rotation angles for the transformation from $|\phi_1\rangle$ to $|\phi_3\rangle$ are provided in Table IV.

As shown in Fig. 7(a), the overlap integral $P^i_{3,1}$ among the initial state, the topological state, and the target state is not large at the first step, but rises to a larger value from the second step. The value of $P^i_{3,1}$ even reaches 0.73 at the eighth step, implying the good support from the constructed topological channel in the transformation. Figure 7(b) depicts the fidelity of $|\phi_3\rangle$. It increases to a high value (>90%) after the first step, which indicates the nearly perfect transformation from the initial state $|\phi_1\rangle$ to $|\phi_3\rangle$. The quantum state tomographies at the fourth and eighth steps are shown in Figs. 7(c) and 7(d), in which the characteristics of the nearly perfect transformation are more clearly observed again. All of the discussions above demonstrate a nearly perfect transformation from $|\phi_1\rangle$ to $|\phi_3\rangle$.

We have also carried out theoretical calculations on the transformation from entangled states $|\phi_1\rangle$ to $|\phi_2\rangle$ ($|\phi_1\rangle$ to

TABLE II. $\theta_{1,\pm}$ and $\theta_{2,\pm}$ of $U_{\text{walk},i}$ for transmission of $|\phi_3\rangle$.

$\|\phi_3\rangle$	$i=1$	$i=2$	$i=3$	$i=4$	$i=5$	$i=6$	$i=7$	$i=8$
$(\theta_{1,+}, \theta_{2,+})$	$(\frac{7\pi}{16}, \frac{6\pi}{16})$	$(\frac{9\pi}{16}, \frac{10\pi}{16})$	$(\frac{-7\pi}{16}, \frac{10\pi}{16})$	$(\frac{7\pi}{16}, \frac{6\pi}{16})$	$(\frac{-7\pi}{16}, \frac{11\pi}{16})$	$(\frac{8\pi}{16}, \frac{6\pi}{16})$	$(\frac{13\pi}{32}, \frac{11\pi}{32})$	$(\frac{-8\pi}{16}, \frac{9\pi}{16})$
$(\theta_{1,-}, \theta_{2,-})$	$(\frac{1\pi}{16}, \frac{7\pi}{16})$	$(\frac{1\pi}{16}, \frac{7\pi}{16})$	$(\frac{6\pi}{16}, \frac{4\pi}{16})$	$(\frac{-1\pi}{16}, \frac{11\pi}{16})$	$(\frac{6.5\pi}{16}, \frac{31\pi}{32})$	$(\frac{3\pi}{32}, \frac{3\pi}{16})$	$(\frac{-25\pi}{32}, \frac{19\pi}{32})$	$(\frac{3\pi}{32}, \frac{14\pi}{16})$

TABLE III. $\theta_{1,\pm}$ and $\theta_{2,\pm}$ of $U_{\text{walk},i}$ for transmission of $\frac{1}{2}|00\rangle + \frac{\sqrt{3}}{2}|11\rangle$.

	$i=1$	$i=2$	$i=3$	$i=4$	$i=5$	$i=6$	$i=7$	$i=8$
$(\theta_{1,+}, \theta_{2,+})$	$(\frac{10\pi}{16}, \frac{8\pi}{16})$	$(\frac{-21\pi}{32}, \frac{-7\pi}{16})$	$(\frac{-9\pi}{16}, \frac{-6\pi}{16})$	$(\frac{-15\pi}{32}, \frac{-11\pi}{16})$	$(\frac{-7\pi}{16}, \frac{-6\pi}{16})$	$(\frac{-19\pi}{32}, \frac{-12\pi}{16})$	$(\frac{8\pi}{16}, \frac{-9\pi}{16})$	$(\frac{-8\pi}{16}, \frac{-7\pi}{16})$
$(\theta_{1,-}, \theta_{2,-})$	$(\frac{9\pi}{16}, \frac{3\pi}{16})$	$(\frac{-4\pi}{16}, \frac{-2\pi}{16})$	$(\frac{13\pi}{16}, \frac{-13\pi}{32})$	$(\frac{13\pi}{32}, \frac{-12\pi}{16})$	$(\frac{-10\pi}{16}, \frac{-9\pi}{16})$	$(\frac{-1\pi}{16}, \frac{-10\pi}{16})$	$(\frac{-12\pi}{16}, \frac{-15\pi}{16})$	$(\frac{-10\pi}{16}, \frac{-9\pi}{16})$

$|\phi_4\rangle$). The inverse design method is also employed. The optimal rotation angles of each step are listed in Table V.

Moreover, the theoretical results of the transformation of entangled states from $|\phi_1\rangle$ to $|\phi_2\rangle$ are shown in Figs. 8(a) and 8(b). The overlap integral $P^i_{2,1}$ has always maintained a high value after the transformation, and the average fidelity of eight steps is equal to 94.9%. Similarly, we also calculated the theoretical results of the transformation from entangled state $|\phi_1\rangle$ to $|\phi_4\rangle$, which are depicted in Figs. 8(c) and 8(d). After the transformation, the value of the overlap integral $P^i_{4,1}$ is well maintained. As the step increases, the fidelity remains high. The average value of fidelity is equal to 92.8%.

APPENDIX C: STRONG LOCALIZATION AT THE TOPOLOGICAL CHANNEL DURING THE TRANSMISSION AND TRANSFORMATION

In our discussion above, we have shown that the fidelity of entangled states keeps a high value during the transmission or transformation. In addition to the high fidelity, the scattering loss can also be controlled to be relatively small and leads to strong localization at the topological channel. Due to the gain effect in the non-Hermitian QW, the summation of probability at each step might be larger than 1 and is called "corrected probability." The blue solid lines in Fig. 9 represent the corrected probability in the topological channel during the transmission. In the nearly perfect transmission of $|\phi_1\rangle$, the localization probabilities in the topological channel are large. When $r = 0.076$, the average value of the localization probability is 0.83 [Fig. 9(a)]. When $r = 0.1$, the average value of the localization probability is 1.09 [Fig. 9(b)]. When the gain-loss strength r increases to 0.2, the mean value of localization probability equals 1.26 [Fig. 9(c)]. It is found that the larger the gain-loss strength, the higher the corrected probability that can be obtained in the topological channel.

Figure 9(d) shows the localization at the topological channel in the transmission of entangled state $|\phi_3\rangle$. The average corrected probability in the topological channel is 0.77. In addition to the maximum entangled state, for the nonmaximum entangled state $\frac{1}{2}|00\rangle + \frac{\sqrt{3}}{2}|11\rangle$, the localization probability at the topological channel is obvious, which is expressed by the blue dots in Fig. 9(e). The mean value of localization over eight steps is approximately 0.48.

In Figs. 10(a)–10(c), we provide the summation of probability at each step with different gain-loss strengths. It is clearly seen that the larger thegain-loss strength, the higher the total corrected probability at each step, which reflects the more obvious gain effect in the non-Hermitian system. We also provide the proportion of corrected probability in the topological channel at each step of QWs. At the eighth step, for these three different gain-loss strengths, the nearly 20% of total corrected probabilities is found in each topological channel [Figs. 10(d)–10(f)]. Considering that the total corrected probability increases with the gain-loss strength, the more corrected probabilities can be found in the topological channel at the larger gain-loss strength. It corresponds to the discussion shown in Figs. 9(a)–9(c).

We also explore the transmission of $|\phi_1\rangle$ with more steps. The inverse design method is employed to find the optimized rotation angles. These rotation angles in the first eight steps are the same as in 1 of Table I. The remaining rotation angles obtained from the inverse design method for the ninth step to the 14th step are listed in Table VI.

In Fig. 11, we show the transmission with 14 steps. Even at the 14th step, the fidelity between the output state and $|\phi_1\rangle$ is larger than 0.8. The fidelity displays an oscillatory behavior and it is not easy to keep a very high value with the step. This is because at the higher steps, more eigenmodes of the system are involved in the transmission at the topological channel, and it is not easy to keep the high fidelity and high efficiency at the same time. With our inverse design, the transmission of $|\phi_1\rangle$ in the topological channel still has high efficiency. The proportion of corrected probability in the topological channel is larger than 20% even at the 14th step.

By using the inverse design method, we can not only realize the perfect transmission of entangled states, but also achieve the nearly perfect transformation of entangled states. For the transformation of entangled states, the initial state and the target state are not the same; $|\phi_l\rangle \neq |\phi_m\rangle$. When the initial state is $|\phi_m\rangle = |\phi_1\rangle = \frac{1}{\sqrt{2}}(|00\rangle + |11\rangle)$ and the target state is $|\phi_l\rangle = |\phi_3\rangle = \frac{1}{\sqrt{2}}(|01\rangle + |10\rangle)$, the average corrected probability in the topological channel shown in Fig. 12(a) is 0.79. Moreover, the theoretical results of the transformation of entangled states from $|\phi_1\rangle$ to $|\phi_2\rangle$ are shown in Fig. 12(b). The average corrected probability in the topological channel is 0.92. Similarly, we also calculated the theoretical results of the transformation from entangled state $|\phi_1\rangle$ to $|\phi_4\rangle$; they are depicted in Fig. 12(c). The average value of

TABLE IV. $\theta_{1,\pm}$ and $\theta_{2,\pm}$ of $U_{\text{walk},i}$ for the transformation from $|\phi_1\rangle$ to $|\phi_3\rangle$.

	$i=1$	$i=2$	$i=3$	$i=4$	$i=5$	$i=6$	$i=7$	$i=8$
$(\theta_{1,+}, \theta_{2,+})$	$(\frac{15\pi}{16}, \frac{4\pi}{16})$	$(\frac{7\pi}{16}, \frac{11\pi}{16})$	$(\frac{7\pi}{16}, \frac{6\pi}{16})$	$(\frac{15\pi}{32}, \frac{11\pi}{16})$	$(\frac{7\pi}{16}, \frac{11\pi}{16})$	$(\frac{9\pi}{16}, \frac{6\pi}{16})$	$(\frac{9\pi}{16}, \frac{10\pi}{16})$	$(\frac{15\pi}{32}, \frac{13\pi}{32})$
$(\theta_{1,-}, \theta_{2,-})$	$(\frac{-15\pi}{16}, \frac{-11\pi}{16})$	$(\frac{7\pi}{32}, \frac{11\pi}{16})$	$(\frac{14\pi}{16}, \frac{25\pi}{32})$	$(\frac{12\pi}{16}, \frac{5\pi}{16})$	$(\frac{11\pi}{32}, \frac{9\pi}{16})$	$(\frac{12\pi}{16}, \frac{11\pi}{32})$	$(\frac{12\pi}{16}, \frac{7\pi}{16})$	$(\frac{-3\pi}{32}, \frac{10\pi}{16})$

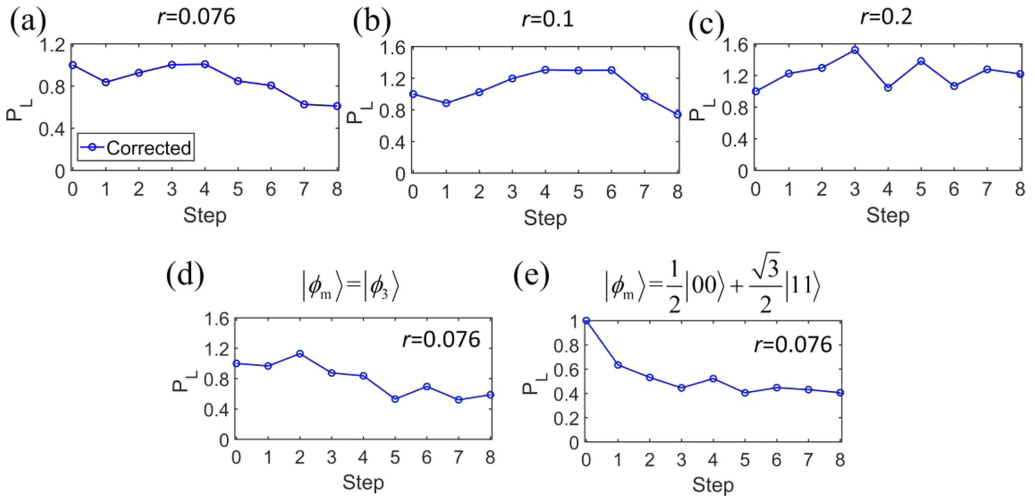

FIG. 9. The localized probability at the topological channel during the transmission. (a–c), the transmission of $|\phi_1\rangle$. (a) $r = 0.076$; (b) $r = 0.1$; (c) $r = 0.2$. (d) The transmission of $|\phi_3\rangle$, $r = 0.076$. (e) The transmission of nonmaximal entangled state $\frac{1}{2}|00\rangle + \frac{\sqrt{3}}{2}|11\rangle$, and $r = 0.076$.

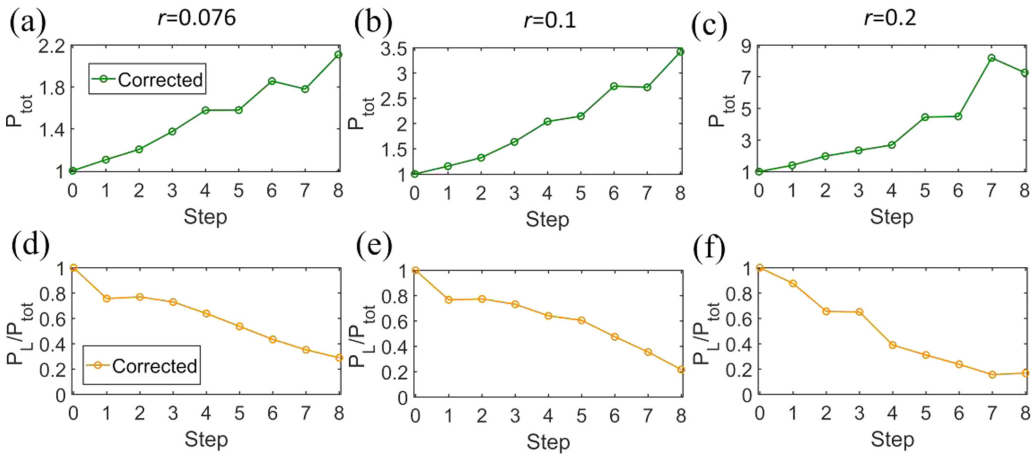

FIG. 10. The corrected probabilities and the proportion in the topological channel during the transmission. (a–c), the total corrected probability in the transmission of $|\phi_1\rangle$. (a) $r = 0.076$; (b) $r = 0.1$; (c) $r = 0.2$. (d–f), the proportion of corrected probability at the topological channel in the transmission of $|\phi_1\rangle$. (d) $r = 0.076$; (e) $r = 0.1$; (f) $r = 0.2$.

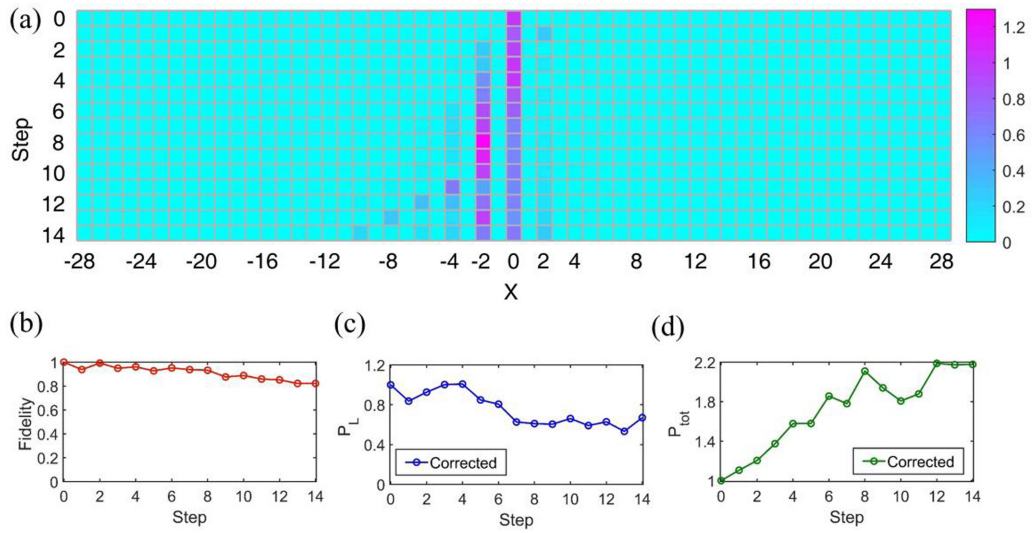

FIG. 11. Theoretical results of more steps for the transmission of $|\phi_1\rangle$. (a) The distribution of corrected probability for 14 steps. (b) The fidelity between the output states and $|\phi_1\rangle$. (c) The corrected probability in the topological channel. (d) The summation of corrected probability at each step. The gain-loss strength $r = 0.076$.

TABLE V. $\theta_{1,\pm}$ and $\theta_{2,\pm}$ of $U_{\text{walk},i}$ for transformation from $|\phi_1\rangle$ to $|\phi_2\rangle$ (1) and transformation from $|\phi_1\rangle$ to $|\phi_4\rangle$ (2).

1	$i=1$	$i=2$	$i=3$	$i=4$	$i=5$	$i=6$	$i=7$	$i=8$
$(\theta_{1,+},\theta_{2,+})$	$(\frac{7\pi}{16},\frac{-15\pi}{16})$	$(\frac{-13\pi}{32},\frac{-31\pi}{32})$	$(\frac{7\pi}{16},\frac{-11\pi}{16})$	$(\frac{17\pi}{32},\frac{10\pi}{16})$	$(\frac{17\pi}{32},\frac{13\pi}{32})$	$(\frac{15\pi}{32},\frac{6\pi}{16})$	$(\frac{7\pi}{16},\frac{25\pi}{32})$	$(\frac{17\pi}{32},\frac{13\pi}{32})$
$(\theta_{1,-},\theta_{2,-})$	$(\frac{-15\pi}{16},\frac{-9\pi}{16})$	$(\frac{-11\pi}{16},\frac{-6\pi}{16})$	$(\frac{-5\pi}{16},\frac{-10\pi}{16})$	$(\frac{5\pi}{16},\frac{15\pi}{32})$	$(\frac{-27\pi}{32},\frac{3\pi}{16})$	$(\frac{-13\pi}{16},\frac{1\pi}{16})$	$(\frac{14\pi}{16},\frac{5\pi}{16})$	$(\frac{12\pi}{16},\frac{10\pi}{16})$
2	$i=1$	$i=2$	$i=3$	$i=4$	$i=5$	$i=6$	$i=7$	$i=8$
$(\theta_{1,+},\theta_{2,+})$	$(\frac{1\pi}{16},\frac{7\pi}{16})$	$(\frac{15\pi}{32},\frac{10\pi}{16})$	$(\frac{15\pi}{32},\frac{13\pi}{32})$	$(\frac{15\pi}{32},\frac{19\pi}{32})$	$(\frac{15\pi}{32},\frac{13\pi}{32})$	$(\frac{-15\pi}{32},\frac{-6\pi}{16})$	$(\frac{17\pi}{32},\frac{6\pi}{16})$	$(\frac{8\pi}{16},\frac{9\pi}{16})$
$(\theta_{1,-},\theta_{2,-})$	$(\frac{-15\pi}{16},\frac{17\pi}{32})$	$(\frac{7\pi}{32},\frac{19\pi}{32})$	$(\frac{1\pi}{16},\frac{11\pi}{16})$	$(\frac{3\pi}{16},\frac{10\pi}{16})$	$(\frac{11\pi}{16},\frac{19\pi}{32})$	$(\frac{1\pi}{32},\frac{-12\pi}{16})$	$(\frac{4\pi}{16},\frac{21\pi}{32})$	$(\frac{-17\pi}{32},\frac{15\pi}{16})$

corrected probability in the topological channel is approximately 0.84.

APPENDIX D: DETAILS OF EXPERIMENTS IN TRANSMISSION AND TRANSFORMATION OF ENTANGLED STATES

The pump source we used is a picosecond pulsed laser from Spectra-Physics, with a center wavelength of 800 nm. After passing through the second harmonic generator (SHG), a pulse of UV light with a central wavelength of 400 nm and an average power of 200 mW is generated. To obtain more entangled photons through the spontaneous parameter down-conversion process, the pulses of light pass through a $4f$ system composed of two lenses with different focal lengths and are finally focused on two noncollinear type-I β-BaB_2O_4 (BBO) crystals, which are vertically pasted together. The thickness of BBO in the experiment is 0.5 mm. A vertically (horizontally) polarized UV light only works in crystal 1(2); the resulting down-conversion light cones are in a horizontally (vertically) polarized state. A 45 °-polarized pump photon is equally likely to down-convert in either crystal, and the photons are automatically created in the state $|HH\rangle + e^{i\alpha}|VV\rangle$. By adjusting the phase of the pump light between the horizontal and vertical polarization components, the maximum polarization entangled state can be prepared.

In the experiment of the non-Hermitian QW, the conditional shift operator is realized by the beam displacer (BD). Due to the birefringence effect, after passing through the BD, a light spot is divided into two light spots with a fixed interval of 3 mm according to different polarization states. By cutting the BD at a specific angle, the horizontally polarized beam can be directly transmitted without changing its transmission direction, while the vertically polarized beam is spatially translated to a grid point 3 mm adjacent to it. In this way, the function of conditional shift operator S can be realized.

For the polarization-dependent loss operators $L = \left(\begin{smallmatrix} l_1 & 0 \\ 0 & l_2 \end{smallmatrix}\right)$ and $L' = \left(\begin{smallmatrix} l_2 & 0 \\ 0 & l_1 \end{smallmatrix}\right)$, a partial polarization beam splitter (PPBS) is used to achieve it. The PPBS is an optical device that has different transmittance $(t_H, t_V) = (l_1^2, l_2^2)$ for the horizontal and vertical polarization of the incident light. In the experiment, the horizontal polarization can be completely transmitted ($t_H = l_1^2 = 1$), while the vertical polarization has a transmittance $t_V = l_2^2$, which achieves polarization-controlled loss operators. The gain-loss strength $r = 1/2\ln(l_1/l_2)$ selected in our experimental program is equal to 0.076, so the corresponding transmittance parameter of our customized PPBS is $(l_1^2, l_2^2) = (1, 0.738)$. Similarly, the loss operator L' can be implemented by the PPBS with another type of transmittance $(t_H, t_V) = (l_2^2, l_1^2)$. To realize this kind of PPBS with special transmittance to polarization, we insert half-wave plates with rotation angles of $\pi/4$ before and after the light is incident on the PPBS. In this way, the loss operator L' can be realized experimentally by the optical device of the sandwich-type HWP-PPBS-HWP combination.

In the experimental construction of the optical platform of the QW, the most important thing is to adjust the cascade interferometer network composed of multiple BDs. To maximize the interference contrast, we need to insert polarization-independent phase shifters in different spatial mode paths. In the experiment, a high-transmittance cover glass can be used to achieve phase adjustment by precisely adjusting the effective thickness of the phase shifters, which is realized by rotating the cover glasses out of the plane perpendicular to the beams. However, the instability of the interferometer under the influence of the external environment during the experiment causes a decrease in the interference visibility. Due to a manufacturing technology problem, each PPBS has a slightly different transmittance for vertically polarized light, which fluctuates approximately 0.738. In addition, after multiple parallel incident lights enter the PPBS, the emergent lights are not at the same height. The imperfect processing of the above-mentioned optical devices causes the final experimental results to be slightly inconsistent with the theoretical results.

In non-Hermitian systems, we have also achieved transmission and transformation with high fidelity of other maximally entangled states; the experimental results of transmission of entangled states $|\phi_3\rangle$ are shown in Figs. 13(a)–13(c). The mean fidelity of the four steps is equal to 91.6%. The

TABLE VI. $\theta_{1,\pm}$ and $\theta_{2,\pm}$ of $U_{\text{walk},i}$ for transmission of $|\phi_1\rangle$ ($r = 0.076$) (1).

1	$i=9$	$i=10$	$i=11$	$i=12$	$i=13$	$i=14$
$(\theta_{1,+},\theta_{2,+})$	$(\frac{-15\pi}{32},\frac{6\pi}{16})$	$(\frac{15\pi}{32},\frac{11\pi}{16})$	$(\frac{17\pi}{32},\frac{6\pi}{16})$	$(\frac{15\pi}{32},\frac{10\pi}{16})$	$(\frac{17\pi}{32},\frac{6\pi}{16})$	$(\frac{17\pi}{32},\frac{10\pi}{16})$
$(\theta_{1,-},\theta_{2,-})$	$(\frac{15\pi}{16},\frac{15\pi}{32})$	$(\frac{-10\pi}{16},\frac{-3\pi}{32})$	$(\frac{-14\pi}{16},\frac{1\pi}{16})$	$(\frac{-14\pi}{16},\frac{3\pi}{16})$	$(\frac{-15\pi}{16},\frac{-1\pi}{32})$	$(\frac{-13\pi}{16},\frac{-1\pi}{32})$

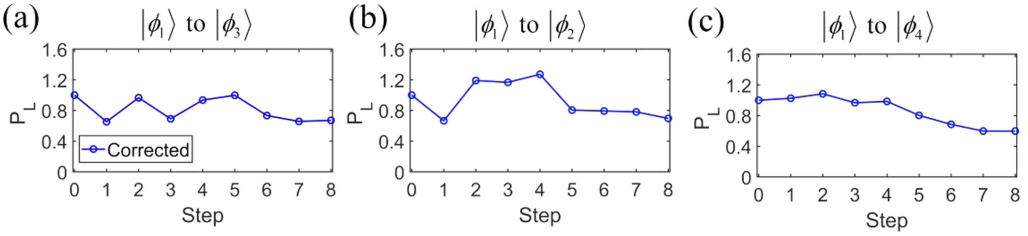

FIG. 12. The corrected probability in the topological channel during the transformation. (a–c), $r = 0.076$. (a) The transformation from $|\phi_1\rangle$ to $|\phi_3\rangle$. (b) The transformation from $|\phi_1\rangle$ to $|\phi_2\rangle$. (c) The transformation from $|\phi_1\rangle$ to $|\phi_4\rangle$.

average corrected probability in the topological channel is 0.97. The quantum state tomography is shown at the fourth step. The similarity $S = 0.934 \pm 0.019$ indicates that the experiments are consistent with the theoretical results. Furthermore, we also experimentally realize the transformation from $|\phi_1\rangle$ to $|\phi_2\rangle$, and the corresponding results are described in Figs. 13(d)–13(f). The entangled state is transformed into $|\phi_2\rangle$ after two steps, and the average fidelity after transformation is approximately 93.9%. The corrected probability in the topological channel averaging over four steps reaches 1.05. The similarity $S = 0.966 \pm 0.008$ shows the excellent agreement between the experimental and theoretical results. In Figs. 13(g)–13(i), the transformation from $|\phi_1\rangle$ to $|\phi_4\rangle$ is addressed. The average fidelity reaches 91.7% after the transformation, and the average value of the corrected probability in the topological channel is 0.89. The similarity $S = 0.946 \pm 0.013$ at the fourth step indicates that the theoretical results are well verified by experimental results.

APPENDIX E: ROBUSTNESS IN THE TRANSMISSION AND TRANSFORMATION OF ENTANGLED STATES

We have tested the robustness of the transmission and transformation of entangled states against disorder in a non-

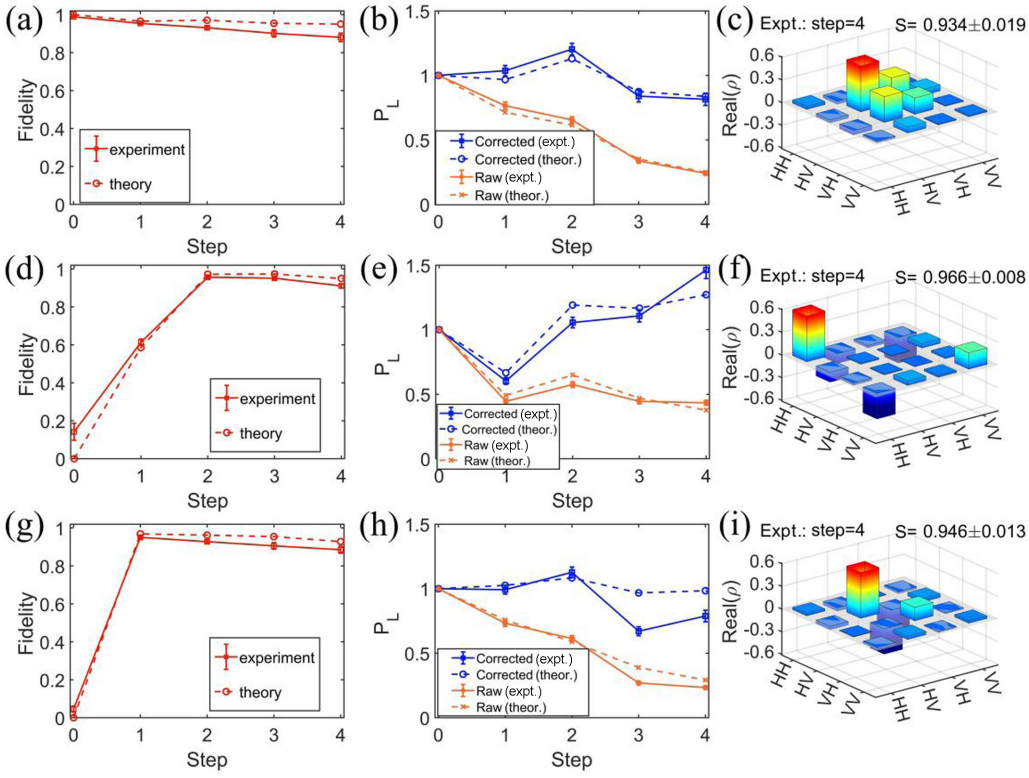

FIG. 13. Experimental results of the transmission and transformation of entangled states. (a–c) Transmission of the entangled state $|\phi_3\rangle$. (d–f) Transformation of entangled states from $|\phi_1\rangle$ to $|\phi_2\rangle$. (g–i) Transformation of entangled states from $|\phi_1\rangle$ to $|\phi_4\rangle$. (a,d,g) The fidelity between the output state and the target states. The red solid (dashed) lines represent the experimental (theoretical) results. (b,e,h) The corrected probability in the topological channel. Orange represents the raw probabilities obtained from the experiment with only loss, and blue represents the corrected probabilities with gain and loss. All error bars refer to ±1 s.d. estimated from Poissonian photon-counting statistics. (c,f,i) The corresponding experimental results of the density matrix at the fourth step. The similarity S is used to indicate the degree of agreement between experiment and theory.

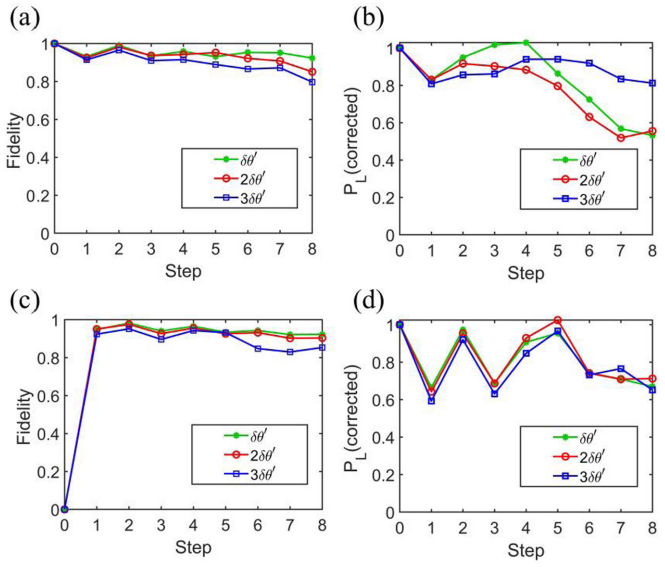

FIG. 14. The transmission and transformation of entangled states in the topological channel. Three different degrees of disorder, $\delta\theta'$, $2\delta\theta'$, and $3\delta\theta'$, are introduced. The transmission results of $|\phi_1\rangle$ are shown in (a,b). (a) The fidelity of $|\phi_1\rangle$ with a step in the presence of disorder. (b) Corrected probabilities in the topological channel with disorder. The transformation results from $|\phi_1\rangle$ to $|\phi_3\rangle$ are presented in (c,d). (c) The fidelity of $|\phi_3\rangle$ with disorder. (d) The corrected probabilities in the topological channel with disorder.

Hermitian system. The results in the main text show that with the introduction of disorder, perfect transmission and transformation of entangled states can also be achieved as in those without disorder. For completeness, we provide the results under the influence of varying degrees of disorder. Three different degrees of disorder, $\delta\theta'$, $2\delta\theta'$, and $3\delta\theta'$, are introduced in the non-Hermitian system, which correspond to the intervals $(-0.031\pi, 0.031\pi)$, $(-0.063\pi, 0.063\pi)$, and $(-0.094\pi, 0.094\pi)$, respectively. The relation between the disorder here $\delta\theta'$ and that in the main text $\delta\theta$ is $\delta\theta = 2\delta\theta'$. Ten different sets of rotation angles are randomly chosen. The results averaging over these ten sets are shown in Fig. 14. In Figs. 14(a) and 14(b), we can find that with the increase in disorder degree, the fidelity of $|\phi_1\rangle$ only decreases slightly and keeps a large value, and the corrected probability in the topological channel is also high. Similarly, in Figs. 14(c) and 14(d), the fidelities and corrected probabilities in the topological channel of transformation from $|\phi_1\rangle$ to $|\phi_3\rangle$ are also obvious, which reveals the robustness of the topologically protected channel against different degrees of disorder.

In our study, we also provide the transmission of entangled state $|\phi_1\rangle$ without a topological channel for comparison. The rotation angles are chosen from the same topological phase for the regions $0 \leqslant x \leqslant N_x$ and $-N_x \leqslant x < 0$, so the channel without the topological protection is created at the interface $x = 0$. In Fig. 15(a), we provide the rotation angles $(\theta_{1,+}, \theta_{2,+}) = (\frac{7\pi}{16}, \frac{4\pi}{16})$ and $(\theta_{1,-}, \theta_{2,-}) = (\frac{4\pi}{16}, \frac{\pi}{32})$ as black and green circles, which are in the same topological phase. The entangled state $|\phi_1\rangle$ is transmitted along this channel. As shown in Figs. 15(b) and 15(c), the fidelity of the output state decreases quickly, accompanied by the very low corrected probability at the nontopologically protected channel. For comparison, when the entangled state $|\phi_1\rangle$ is transmitted along the topological channel, the fidelity of the output state at the eighth step is about 0.95 [Fig. 4(a)] and the corrected probability in the topological channel at the eighth step is higher than 0.6 [Fig. 9(a)].

Moreover, we also discuss the transmission of entangled state $|\phi_1\rangle$ with the presence of disorder. In Figs. 15(b) and 15(c), the static disorder in the system is introduced by adding random angles $2\delta\theta'$ and $3\delta\theta'$ to θ_1 and θ_2 as $(\theta_{1,\pm} + 2\delta\theta', \theta_{2,\pm} + 2\delta\theta')$ and $(\theta_{1,\pm} + 3\delta\theta', \theta_{2,\pm} + 3\delta\theta')$, respectively. The degree of disorder $\delta\theta'$ is chosen randomly from the interval $(-0.031\pi, 0.031\pi)$ in a uniform distribution. It is found that the fidelity of the output states and the corrected probabilities in the nontopologically protected channel are also small. As a comparison, even in the presence of disorder, the fidelities in the transmission of entangled state $|\phi_1\rangle$ at the topological channel are very large, and the corrected probabilities in the topological channel are also obvious; see Fig. 14.

Based on such comparisons above, we can conclude that we have designed topologically protected channels according to our proposed inverse design scheme and realized nearly perfect transmission and transformation of entangled states. Our scheme is able to combine the advantages from topology

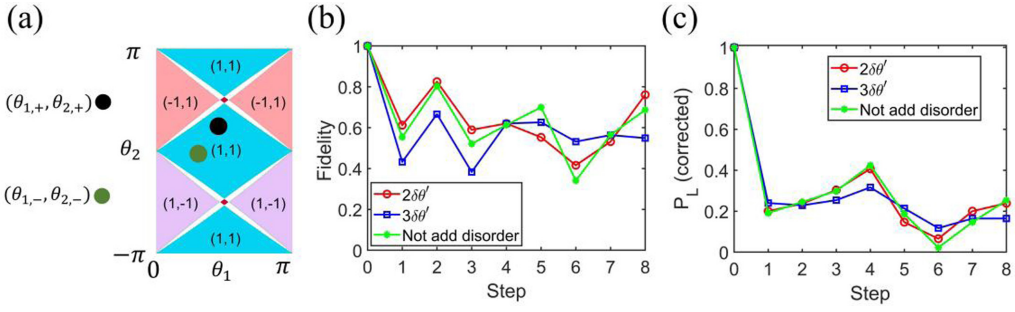

FIG. 15. The transmission of $|\phi_1\rangle$ in the non-Hermitian QW without the topological channel. (a) Rotation angles in the regions $0 \leqslant x \leqslant N_x$ and $-N_x \leqslant x < 0$ are $(\theta_{1,+}, \theta_{2,+}) = (\frac{7\pi}{16}, \frac{4\pi}{16})$ and $(\theta_{1,-}, \theta_{2,-}) = (\frac{4\pi}{16}, -\frac{\pi}{32})$, respectively. These two sets of rotation angles are labeled as black and green circles. (b) The fidelity in the transmission of $|\phi_1\rangle$ with a step. (c) The corrected probability at the position $x = 0$. (b,c) Green, without disorder; red, the disorder $2\delta\theta'$ introduced; blue, the disorder $3\delta\theta'$ introduced. The gain-loss strength $r = 0.076$.

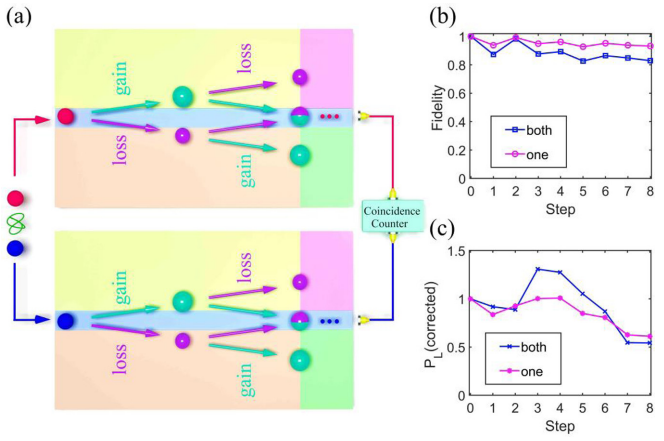

FIG. 16. Evolution of entangled states in a non-Hermitian system. (a) Transmission of entangled states in topological channels. One part of the entangled state passes through the topological channel, and the other also travels in the same topological channel. (b) The fidelity between the output state and $|\phi_1\rangle$. (c) The corrected probabilities in the topological channels. The blue dots represent the case in which both parts of the entangled state enter the topological channels. The pink dots represent the case in which one part of the entangled state enters the topological channel, and the other one travels in vacuum.

and special design in maintaining high fidelity and high efficiency for entangled states during the evolution.

APPENDIX F: TRANSMISSION FOR BOTH PARTS OF ENTANGLED STATES ENTERING INTO TOPOLOGICAL CHANNELS

Another situation is considered in which both parts of the entangled state enter the topological channel [Fig. 16(a)]. The perfect transmission of entangled state $|\phi_1\rangle$ is also verified. The rotation angles are same as those used in Fig. 4. The fidelities and the corrected probabilities in the topological channel are represented by blue dots in Figs. 16(b) and 16(c), respectively. For comparison, pink dots are used to represent the results in Figs. 4(a) and 9(a). It can be seen that when both parts of the entangled state enter the topological channels, the fidelity of the entangled state $|\phi_1\rangle$ still maintains a high value and propagates almost unchanged. In addition, the corrected probabilities in the topological channel are also large. The discussion above indicates that even when both parts of the entangled state enter the topological channels, the perfect transmission of the entangled state in the non-Hermitian system can also be achieved by using our inverse design method.

[1] T. D. Ladd, F. Jelezko, R. Laflamme, Y. Nakamura, C. Monroe and J. L. O'Brien, Quantum computers, Nature (London) **464**, 45 (2010).

[2] J. W. Pan, Z. B. Chen, C. Y. Lu, H. Weinfurter, A. Zeilinger, and M. Żukowski, Multiphoton entanglement and interferometry, Rev. Mod. Phys. **84**, 777 (2012).

[3] L. Lu, J. D. Joannopoulos, and M. Soljacic, Topological Photonics, Nat. Photonics **8**, 821 (2014).

[4] T. Ozawa, H. M. Price, A. Amo, N. Goldman, M. Hafezi, L. Lu, M. C. Rechtsman, D. Schuster, J. Simon, O. Zilberberg, and I. Carusotto, Topological photonics, Rev. Mod. Phys. **91**, 015006 (2019).

[5] S. Mittal, V. V. Orre, and M. Hafezi, Topologically robust transport of entangled photons in a 2D photonic system, Opt. Express **24**, 15631 (2016).

[6] M. C. Rechtsman, Y. Lumer, Y. Plotnik, A. Perez-Leija, A. Szameit, and Mordechai Segev, Topological protection of photonic path entanglement, Optica **3**, 925 (2016).

[7] J. Perczel, J. Borregaard, D. E. Chang, H. Pichler, S. F. Yelin, P. Zoller, and M. D. Lukin, Topological Quantum Optics in Two-Dimensional Atomic Arrays, Phys. Rev. Lett. **119**, 023603 (2017).

[8] S. Barik, A. Karasahin, C. Flower, T. Cai, H. Miyake, W. DeGottardi, M. Hafezi, and E. Waks, A topological quantum optics interface, Science **359**, 666 (2018).

[9] S. Mittal, E. A. Goldschmidt, and M. Hafezi, A topological source of quantum light, Nature (London) **561**, 502 (2018).

[10] J.-L. Tambasco, G. Corrielli, R. J. Chapman, A. Crespi, O. Zilberberg, R. Osellame, and A. Peruzzo, Quantum interference of topological states of light, Sci. Adv. **4**, eaat3187 (2018).

[11] A. Blanco-Redondo, B. Bell, D. Oren, B. J. Eggleton, and M. Segev, Topological protection of biphoton states, Science **362**, 568 (2018).

[12] S. Molesky, Z. Lin, A. Y. Piggott, W. Jin, J. Vuckovic, and A. W. Rodriguez, Inverse design in nanophotonics, Nat. Photonics **12**, 659 (2018).

[13] K. Yao, D. R. Unni, and Y. Zheng, Intelligent nanophotonics: Merging photonics and artificial intelligence at the nanoscale, Nanophotonics **8**, 339 (2019).

[14] Y. Wang, X.-L. Pang, Y.-H. Lu, J. Gao, Y.-J. Chang, L.-F. Qiao, Z.-Q. Jiao, H. Tang, and X.-M. Jin, Topological protection of two-photon quantum correlation on a photonic chip, Optica **6**, 955 (2019).

[15] T. Giordani, E. Polino, S. Emiliani, A. Suprano, L. Innocenti, H. Majury, L. Marrucci, M. Paternostro, A Ferraro, N. Spagnolo, and F. Sciarrino, Experimental Engineering of Arbitrary Qudit States with Discrete-Time Quantum Walks, Phys. Rev. Lett. **122**, 020503 (2019).

[16] L. Su, D. Vercruysse, J. Skarda, N. V. Sapra, J. A.Petykiewicz, and J. Vu kovi, Nanophotonic inverse design with SPINS: Software architecture and practical considerations, Appl. Phys. Rev. **7**, 011407 (2020).

[17] J. Perczel, J. Borregaard, D. E. Chang, S. F. Yelin, and M. D. Lukin, Topological Quantum Optics Using Atomlike Emitter Arrays Coupled to Photonic Crystals, Phys. Rev. Lett. **124**, 083603 (2020).

[18] K. Tschernig, A. Jimenez-Galán, D. N. Christodoulides, M. Ivanov, K. Busch, M. A. Bandres, and A. Perez-Leija, Topological protection versus degree of entanglement of two-photon light in photonic topological insulators, Nat. Commun. **12**, 1974 (2021).

[19] B. Wang, Z. Tang, T. Chen, and X. Zhang, Nearly perfect transmission and transformation of entangled states in topologically protected channels, Laser Photonics Rev. **16**, 2100519 (2022).

[20] Y. Wang, Y.-H. Lu, J. Gao, Y.-J. Chang, R.-J. Ren, Z.-Q. Jiao, Z.-Y. Zhang, X.-M. Jin, Topologically protected polarization quantum entanglement on a photonic chip, Chip **1**, 100003 (2022).

[21] N. Moiseyev, *Non-Hermitian Quantum Mechanics* (Cambridge University Press, Cambridge, 2011).

[22] R. EI-Ganainy, K. G. Makris, M. Khajavikhan, Z. H. Musslimani, S. Rotter, and D. N. Christodoulides, Non-Hermitian physics and $\mathcal{PT}$ symmetry, Nat. Phys. **14**, 11 (2018).

[23] T. A. Brun, H. A. Carteret, and A. Ambainis, Quantum to Classical Transition for Random Walks, Phys. Rev. Lett. **91**, 130602 (2003).

[24] D. Shapira, O. Biham, A. J. Bracken, and M. Hackett, One-dimensional quantum walk with unitary noise, Phys. Rev. A **68**, 062315 (2003).

[25] C. Oliveira, R. Portugal, and R. Donangelo, Decoherence in two-dimensional quantum walks, Phys. Rev. A **74**, 012312 (2006).

[26] V. Kendon, Decoherence in quantum walks—a review, Math. Struct. Comput. Sci. **17**, 1169 (2007).

[27] H. B. Perets, Y. Lahini, F. Pozzi, M. Sorel, R. Morandotti, and Y. Silberberg, Realization of Quantum Walks with Negligible Decoherence in Waveguide Lattices, Phys. Rev. Lett. **100**, 170506 (2008).

[28] A. Schreiber, K. N. Cassemiro, V. Potoček, A. Gábris, P. J. Mosley, E. Andersson, I. Jex, and C. Silberhorn, Photons Walking the Line: A Quantum Walk with Adjustable Coin Operations, Phys. Rev. Lett. **104**, 050502 (2010).

[29] A. Schreiber, K. N. Cassemiro, V. Potoček, A. Gábris, I. Jex, and C. Silberhorn, Decoherence and Disorder in Quantum Walks: From Ballistic Spread to Localization, Phys. Rev. Lett. **106**, 180403 (2011).

[30] P. Xue and B. C. Sanders, Controlling and reversing the transition from classical diffusive to quantum ballistic transport in a quantum walk by driving the coin, Phys. Rev. A **87**, 022334 (2013).

[31] T. E. Lee, Anomalous Edge State in a Non-Hermitian Lattice, Phys. Rev. Lett. **116**, 133903 (2016).

[32] S. Weimann, M. Kremer, Y. Plotnik, Y. Lumer, S. Nolte, K. G. Makris, M. Segev, M. C. Rechtsman, and A. Szameit, Topologically protected bound states in photonic parity–time-symmetric crystals, Nat. Mater. **16**, 433 (2017).

[33] L. Xiao, X. Zhan, Z. H. Bian, K. K. Wang, X. Zhang, X. P. Wang, J. Li, K. Mochizuki, D. Kim, N. Kawakami *et al.*, Observation of topological edge states in parity–time-symmetric quantum walks, Nat. Phys. **13**, 1117 (2017).

[34] S. Yao and Z. Wang, Edge States and Topological Invariants of Non-Hermitian Systems, Phys. Rev. Lett. **121**, 086803 (2018).

[35] H. Shen, B. Zhen, and L. Fu, Topological Band Theory for Non-Hermitian Hamiltonians, Phys. Rev. Lett. **120**, 146402 (2018).

[36] Z. Gong, Y. Ashida, K. Kawabata, K. Takasan, S. Higashikawa, and M. Ueda, Topological Phases of Non-Hermitian Systems, Phys. Rev. X **8**, 031079 (2018).

[37] M.-A. Miri and A. Alù, Exceptional points in optics and photonics, Science **363**, 7709 (2019).

[38] K. Kawabata, K. Shiozaki, M. Ueda, and M. Sato, Symmetry and Topology in Non-Hermitian Physics, Phys. Rev. X **9**, 041015 (2019).

[39] N. Okuma, K. Kawabata, K. Shiozaki, and M. Sato, Topological Origin of Non-Hermitian Skin Effects, Phys. Rev. Lett. **124**, 086801 (2020).

[40] D. S. Borgnia, A. J. Kruchkov, and R.-J. Slager, Non-Hermitian Boundary Modes and Topology, Phys. Rev. Lett. **124**, 056802 (2020).

[41] K. Zhang, Z. Yang, and C. Fang, Correspondence between Winding Numbers and Skin Modes in Non-Hermitian Systems, Phys. Rev. Lett. **125**, 126402 (2020).

[42] L. Xiao, T. Deng, K. Wang, G. Zhu, Z. Wang, W. Yi, and P. Xue, Observation of non-Hermitian bulk-boundary correspondence in quantum dynamics, Nat. Phys. **16**, 761 (2020).

[43] T. Helbig, T. Hofmann, S. Imhof, M. Abdelghany, T. Kiessling, L. W. Molenkamp, C. H. Lee, A. Szameit, M. Greiter and R. Thomale, Generalized bulk-boundary correspondence in non-Hermitian topolectrical circuits, Nat. Phys. **16**, 747 (2020).

[44] A. Ghatak, M. Brandenbourger, J. van Wezel, and C. Coulais, Observation of non-Hermitian topology and its bulk-edge correspondence, Proc. Natl Acad. Sci. USA **117**, 29561 (2020).

[45] B. Wang, T. Chen, and X. Zhang, Observation of novel robust edge states in dissipative non-hermitian quantum walks, Laser Photonics Rev. **14**, 2000092 (2020).

[46] E. J. Bergholtz, J. C. Budich, and F. K. Kunst, Exceptional topology of non-Hermitian systems, Rev. Mod. Phys. **93**, 015005 (2021).

[47] L. S. Palacios, S. Tchoumakov, M. Guix, I. Pagonabarraga, S. Sánchez, and A. G Grushin, Guided accumulation of active particles by topological design of a second-order skin effect, Nat. Commun. **12**, 4691 (2021).

[48] L. Li, C. H. Lee, and J. Gong, Topological Switch for Non-Hermitian Skin Effect in Cold-Atom Systems with Loss, Phys. Rev. Lett. **124**, 250402 (2020).

[49] D. Zou, T. Chen, W. He, J. Bao, C. H. Lee, H. Sun, and X. Zhang, Observation of hybrid higher-order skin-topological effect in non-Hermitian topolectrical circuits, Nat. Commun. **12**, 7201 (2021).

[50] P. S.-Jean, V. Goblot, E. Galopin, A. Lemaître, T. Ozawa, L. Le Gratiet, I. Sagnes, J. Bloch and A. Amo, Lasing in topological edge states of a one-dimensional lattice, Nat. Photonics **11**, 651 (2017).

[51] H. Zhao, P. Miao, M. H. Teimourpour, S. Malzard, R. ElGanainy, H. Schomerus, and L. Feng, Topological hybrid silicon microlasers, Nat. Commun. **9**, 981 (2018).

[52] G. Harari, M. A. Bandres, Y. Lumer, M. C. Rechtsman, Y. D. Chong, M. Khajavikhan, D. N. Christodoulides, and M. Segev, Topological insulator laser: Theory, Science **359**, 1230 (2018).

[53] M. A. Bandres, M. A. Bandres, Y. Lumer, M. C. Rechtsman, Y. D. Chong, M. Khajavikhan, D. N. Christodoulides, and M. Segev, Topological insulator laser: Experiments, Science **359**, 1231 (2018).

[54] W. Zhang, X. Xie, H. Hao, J. Dang, S. Xiao, S. Shi, H. Ni, Z. Niu, C. Wang, K. Jin, X. Zhang, and X. Xu, Low-threshold topological nanolasers based on the second order corner state, Light: Sci. Appl. **9**, 109 (2020).

[55] K. Mochizuki, D. Kim, and H. Obuse, Explicit definition of $\mathcal{PT}$ symmetry for nonunitary quantum walks with gain and loss, Phys. Rev. A **93**, 062116 (2016).

[56] T. Chen, B. Wang, and X. Zhang, Characterization of topological phases and selection of topological interface modes in the parity-time-symmetric quantum walk, Phys. Rev. A **97**, 052117 (2018).

[57] K. Manouchehri and J. B. Wang, *Physical Implementation of Quantum Walks* (Springer, Berlin, 2014).

[58] R. Portugal, *Quantum Walks and Search Algorithms* (Springer, Cham, Switzerland, 2018).

[59] A. M. Childs, Universal Computation by Quantum Walk, Phys. Rev. Lett. **102**, 180501 (2009).

[60] A. Schreiber, A. Gábris, P. P. Rohde, K. Laiho, M. Štefanák, V. Potocek, C. Hamilton, I. Jex, and C. Silberhorn, A 2D quantum walk simulation of two-particle dynamics, Science **336**, 55 (2012).

[61] A. M. Childs, D. Gosset, and Z. Webb, Universal computation by multiparticle quantum walk, Science **339**, 791 (2013).

[62] A. Crespi, R. Osellame, R. Ramponi, V. Giovannetti, R. Fazio, L. Sansoni, F. De Nicola, F. Sciarrino, and P. Mataloni, Anderson localization of entangled photons in an integrated quantum walk, Nat. Photonics **7**, 322 (2013).

[63] F. De Nicola, L. Sansoni, A. Crespi, R. Ramponi, R. Osellame, V. Giovannetti, R. Fazio, P. Mataloni, and F. Sciarrino, Quantum simulation of bosonic-fermionic noninteracting particles in disordered systems via a quantum walk, Phys. Rev. A **89**, 032322 (2014).

[64] D. A. Meyer and T. G. Wong, Connectivity is a Poor Indicator of Fast Quantum Search, Phys. Rev. Lett. **114**, 110503 (2015).

[65] T. Rakovszky and J. K. Asboth, Localization, delocalization, and topological phase transitions in the one-dimensional split-step quantum walk, Phys. Rev. A **92**, 052311 (2015).

[66] J. K. Asboth and J. M. Edge, Edge-state-enhanced transport in a two-dimensional quantum walk, Phys. Rev. A **91**, 022324 (2015).

[67] S. Chakraborty, L. Novo, A. Ambainis, and Y. Omar, Spatial Search by Quantum Walk is Optimal for Almost All Graphs, Phys. Rev. Lett. **116**, 100501 (2016).

[68] D. N. Biggerstaff, R. Heilmann, A. A. Zecevik, M. Gräfe, M. A. Broome, A. Fedrizzi, S. Nolte, A. Szameit, A. G. White, and I. Kassal, Enhancing coherent transport in a photonic network using controllable decoherence, Nat. Commun. **7**, 11282 (2016).

[69] X. Qiang, T. Loke, A. Montanaro, K. Aungskunsiri, X. Zhou, J. L. O'Brien, J. B. Wang, and J. C. F. Matthews, Efficient quantum walk on a quantum processor, Nat. Commun. **7**, 11511 (2016).

[70] L. Innocenti, H. Majury, T. Giordani, N. Spagnolo, F. Sciarrino, M. Paternostro, and A. Ferraro, Quantum state engineering using one-dimensional discrete-time quantum walks, Phys. Rev. A **96**, 062326 (2017).

[71] H. Tang, C. Di Franco, Z.-Y. Shi, T.-S. He, Z. Feng, J. Gao, K. Sun, Z.-M. Li, Z.-Q. Jiao, T.-Y. Wang *et al.*, Experimental quantum fast hitting on hexagonal graphs, Nat. Photonics **12**, 754 (2018).

[72] A. Montanaro, Quantum-walk speedup of backtracking algorithms, Theor. Comput. **14**, 1 (2018).

[73] T. Wu, J. A. Izaac, Z.-X. Li, K. Wang, Z.-Z. Chen, S. Zhu, J. B. Wang, and X.-S. Ma, Experimental Parity-Time Symmetric Quantum Walks for Centrality Ranking on Directed Graphs, Phys. Rev. Lett. **125**, 240501 (2020).

[74] X. Qiang, Y. Wang, S. Xue, R. Ge, L. Chen, Y. Liu, A. Huang, X. Fu, P. Xu, T. Yi *et al.*, Implementing graph-theoretic quantum algorithms on a silicon photonic quantum walk processor, Sci. Adv. **7**, eabb8375 (2021).